Anisotropic tensile failure of metals by the strain localization theory: an application to a high-strength aluminium alloy

D. Morin[a,b], M. Fourmeau[a,c], T. Børvik[a,b], A. Benallal[d], O. S. Hopperstad[a,b]

[a] *Centre for Advanced Structural Analysis (CASA), Norwegian University of Science and Technology (NTNU), NO-7491 Trondheim, Norway*
[b] *Structural Impact Laboratory (SIMLab), Department of Structural Engineering, NTNU, NO-7491 Trondheim, Norway*
[c] *SINTEF Materials Chemistry, NO-7465 Trondheim, Norway*
[d] *Laboratoire de Mecanique et Technologie, ENS Cachan/CNRS/Universite Paris-Saclay, Cachan, France*

Abstract

This paper investigates the influence of plastic anisotropy on the tensile ductility of a high-strength aluminium alloy. To this end, finite element simulations of smooth and notched tension tests in different material directions are performed with an anisotropic plasticity model. The stress and strain histories from these simulations are then applied in localization analyses with the imperfection band approach, using the anisotropic plasticity model outside the band and an anisotropic version of the Gurson model inside the band. The imperfection within the band is represented by a volume fraction of void nucleating particles. The high-strength aluminium alloy AA7075-T651 is considered in this study. The results show that the directional dependency of the tensile ductility of the alloy found experimentally is predicted with good accuracy using the adopted approach. The numerical study indicates that plastic anisotropy plays an important role in determining the anisotropic tensile ductility of this high-strength aluminium alloy.

Keywords: Localization, anisotropic ductile failure, porous plasticity, aluminium alloys

1. Introduction

This paper is concerned with the roles played by anisotropy in the failure process of a high-strength aluminium alloy. More precisely, the aim of the current study is to evaluate to which extent the observed anisotropy in tensile ductility of a high-strength, age-hardened aluminium alloy can be ascribed to plastic anisotropy.

The anisotropy of aluminium alloys stems from the manufacturing process. Extruded profiles, rolled plates and plastically formed structural components invariably exhibit anisotropy, but the strength of the anisotropy varies. The plastic anisotropy with regards to yielding and plastic flow is mostly governed by the crystallographic texture, and is, at least qualitatively, well described by crystal plasticity [1, 2, 3]. In phenomenological models, the plastic anisotropy in yielding and plastic flow is described by an anisotropic yield surface [4, 5, 6], while the ductility of aluminium alloys depends on several factors. It has been found experimentally that the tensile ductility decreases with increasing yield stress [7, 8, 9]. Simulations indicate that this finding is partially due to changes in the deformation pattern and stress state in the necked region of the tensile specimen, since higher yield strength usually correlates with reduced work hardening [10]. The main microstructural feature known to influence ductility is the distribution of second-phase particles or inclusions [11]. The mechanism of ductile failure consists of nucleation, growth and coalescence of voids around these particles. These processes have been shown to depend markedly on the stress state, often represented by the stress triaxiality and the Lode angle [12]. If the particles are present as stringers along the rolling or extrusion direction, the result is anisotropic damage evolution and failure [13, 14, 15].

Another micro-structural feature found to influence particularly the toughness of age-hardening aluminium alloys is the precipitate-free zones along the grain boundaries [16, 17]. These alloys get their strength from a high density of small hardening precip-

itates which are formed during artificial ageing of the alloy. However, narrow regions around the grain boundaries are free of hardening precipitates and thus act as soft zones in which deformations tend to localize [18]. The main trend found experimentally is that precipitate-free zones in high-strength aluminium alloys increase the propensity for inter-granular fracture which decreases the toughness of the alloy [16, 17]. If the grains are elongated as a result of the extrusion or rolling process, grain boundary failure could induce anisotropy in the failure strain. Another source of anisotropic tensile ductility is the plastic anisotropy, because it changes the stress level and the plastic flow of the material with loading direction.

Ductile failure has been widely investigated in the literature using different techniques. Hybrid experimental and numerical approaches have been successfully employed by several authors, among them, Bao and Wierzbicki [19], Barsoum and Faleskog [20], Li et al. [21] and Gruben et al. [22] investigated ductile failure in aluminium alloys and advanced high strength steels under a wide range of stress states. With the recent increase in computational power, unit cell simulations have become an attractive way to study ductile failure[23, 24, 25, 26]. These simulations enable the study of the local deformation fields and can provide a deeper knowledge of the growth and coalescence of voids. Unit cell simulations have also been employed to study strain localization phenomena, as for instance in Barsoum and Faleskog [27, 28], Dunand and Mohr [12] and Tekoglu et al. [29]. These analyses have been employed to highlight and confirm several experimental observations such as the influence of the Lode parameter on ductile failure. Studies employing an anisotropic matrix material are more scarce. Some noticable studies are those of Benzerga and Besson [30], Chien et al. [31], Wang et al. [32], Steglich et al. [33], Keralavarma and Benzerga [23, 34] and Dæhli et al. [35], in which unit cell simulations were used to investigate void growth and coalescence in a homogeneized anisotropic matrix and typically compared to anisotropic porous plasticity models. To

the authors' best knowledge, strain localization analyses employing unit cell simulations with an anisotropic matrix material have not yet been reported in the literature. Despite the increase in computational power, strain localization analyses using such unit cells are still difficult to carry out. The orientation of the localization band cannot be restricted to a 2D setup (as in [27, 28, 12, 29]) and a large number of orientations should be investigated within a 3D setup, thus leading to prohibitive computational times.

Two widely accepted ideas on the characteristics of structural materials are adopted in this paper. On the one hand, real materials are usually not homogeneous and contain various types of non-uniformities such as particles and voids. On the other hand, it is generally observed that inelastic phenomena, such as plastic deformation and/or damage evolution, localize into small zones prior to failure initiation. As shown by Tekoglu et al. [29], localization occurs either simultaneously or prior to void coalescence depending on the stress triaxiality. Thus, the localization phenomenon can be considered in many instances to be a precursor to and a severe warning against initiation of ductile failure.

Apart from unit cell simulations, strain localization phenomena have been widely studied in the literature. Marciniak and Kuczynski [36] used the possibly pre-existing non-uniformities to explain localized necking in sheets deformed in biaxial tension. The introduction of inhomogeneities in the sheet material allowed for the development of a local neck. Rudnicki and Rice [37] discussed the conditions for the localization of plastic deformation in plastically dilatant materials with pressure sensitive yielding for homogeneous materials. In that study, localization was investigated as a bifurcation and they found that materials are resistant to such bifurcation localization for axisymmetric extension or compression types of loadings. Rice reconsidered the localization conditions in a more general context in [38], where he also introduced the idea of Marciniak and Kuczynski [36], putting this approach into a general and rigorous formulation. Yamamoto [39], Needleman and Rice [40], Saje et al. [41], Pan et al. [42], Mear and

Hutchinson [43], Tvergaard and Needleman [44], Nahshon and Hutchinson [45], Gruben et al. [46] and Morin et al. [47] used this formulation in various contexts with the common objective of removing the resistant character of localization for homogeneous materials. The idea is that the presence of an imperfection with slightly different properties from the rest of the material leads to a concentration of strain within this imperfection and promotes localization in the material. The same idea has long been used to obtain realistic buckling loads both in elastic and plastic ranges by introducing imperfections [48, 49, 50, 51]. As shown by Morin et al. [47] and Dæhli et al. [52], strain localization analyses using the imperfection approach [38] are able to provide good qualitative, and reasonable quantitative, agreement with unit cell simulations in terms of predicted ductility. The computational efficiency of the strain localization analyses relaxes the restriction on the number of band orientations investigated when studying localization in anisotropic materials.

This study extend a framework presented by Gruben et al. [46] and Morin et al. [47] to anisotropic aluminium alloys by incorporating plastic anisotropy into the strain localization analyses. The general theoretical framework proposed by Rice [38] is employed to predict the initiation of ductile failure. Based on this framework, the imperfection is taken in the form of a planar band. For a given loading process, the constitutive equations lead to homogeneous states inside and outside the planar band while finite discontinuities of the deformation fields can occur at the interface. Strain localization is here defined by the loss of ellipticity of the governing equations inside the imperfection band. At localization by loss of ellipticity, the rate-of-deformation field becomes infinite inside the imperfection band whereas it is finite outside. Beside its planar geometry, the imperfection must also be characterized with respect to its constitutive behaviour. This can be done in a number of ways, but all need to incorporate a softening mechanism [37] in order to trigger loss of ellipticity in the framework of associative inelastic behaviour,

which is considered in the paper. In the context of initiation of ductile fracture, as envisaged here, a natural choice is void nucleation and growth where these voids generally arise from cracking of second-phase particles, such as inclusions, dispersoids and precipitates, or from decohesion at particle-matrix interfaces [11], even if other processes can be in play. The Gurson model [53] is used here with some of its improvements as proposed by Tvergaard [54] and by Chu and Needlemann [55] with the nucleation of voids. In addition, the plastic anisotropy of the matrix material is heuristically accounted for by modifying the definition of the equivalent stress [35]. While strain localization analyses, using the imperfection approach, are computationally efficient [47], their predictions are strongly dependent upon the constitutive equations used inside the imperfection band. Nevertheless, the important question of how the predicted failure properties depend on the choice of the imperfection and its material properties is not considered in this study. As done by Gruben et al. [46] and in most of the simulations of Nahshon and Hutchinson [45], the material outside the imperfection band is considered to be sound (void free) and described by an anisotropic metal plasticity model. Here, we have implicitly assumed that all damage evolution is confined to the imperfection band and that any damage mechanism outside the band is negligible. This is a rather strong assumption, but should lead to conservative estimates of the ductility in the framework of an imperfection analysis. Thus, ductile failure is considered to initiate when loss of ellipticity is detected within the imperfection band. An illustration of the methodology applied in this study is given in Figure 1. Finite element simulations of tensile tests are conducted using metal plasticity. The deformation histories for all elements within the minimum cross-section of the specimen are extracted and used in localization analyses. The overall failure strain is determined by the element first reaching localization. This way, both the strain to failure and the location of failure initiation are predicted. A more detailed presentation of the methodology is given in Section 5.2.

In the next section, a brief description of the investigated aluminium alloy together with the experimental programme designed to exhibit its failure properties is given. Section 3 presents the Gurson model modified heuristically to account for plastic anisotropy, while Section 4 briefly describes the localization analysis in the presence of an imperfection band. Section 5 is devoted to the numerical implementation of the localization approach and the details of the numerical procedures used to construct the failure loci. The results of the numerical study are presented, compared with the experimental findings and discussed in Section 6, while Sections 7 provides some concluding remarks.

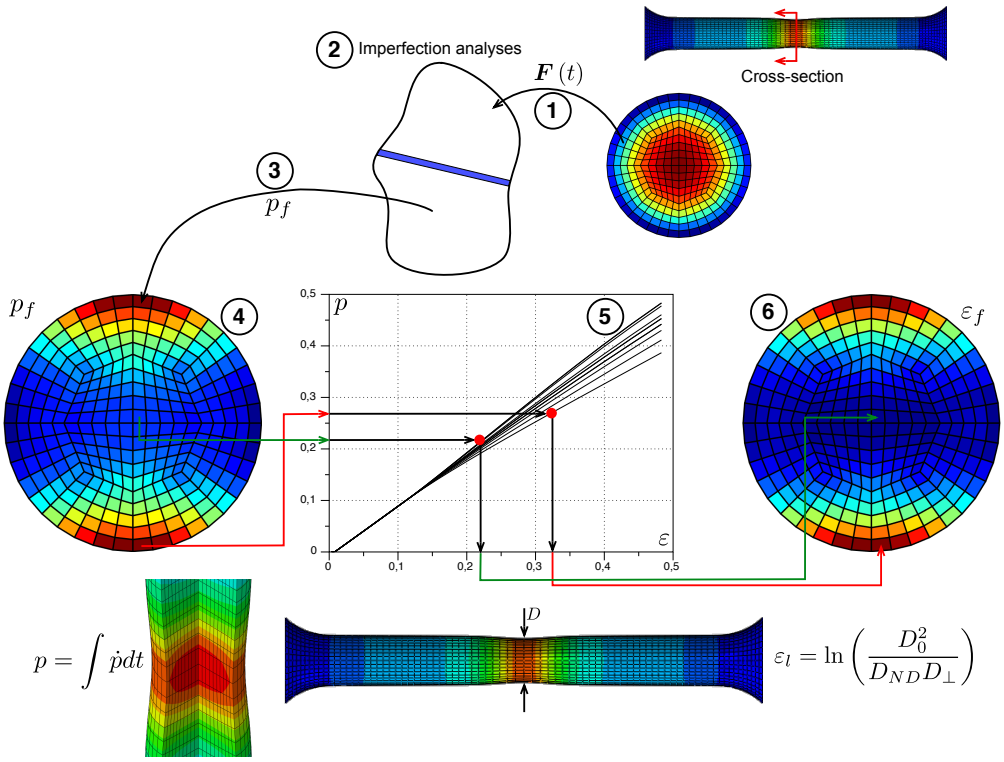

Figure 1: Methodology of the localization analyses: the deformation gradients $\boldsymbol{F}(t)$ of each element (obtained by a preliminary finite element analysis) within the minimum cross-section ① are used to carry out an imperfection analysis ② to find the local equivalent plastic strains at localization p_f (③, ④) and the macroscopic failure strains ε_f (⑤, ⑥) are mapped onto the initial cross section using the relationship between the local equivalent plastic strains p and the logarithmic strain ε_l.

2. Summary of previous experimental study

The material considered in this study is a 20-mm thick rolled plate of the high-strength aluminium alloy AA7075-T651. Temper T651 implies that the material is artificially aged to peak hardness and subsequently stress relieved by slight stretching, while the combined cold and hot rolling process gives a crystallographic texture that leads to anisotropic characteristics. The bulk of the AA7075-T651 alloy has a complex non-recrystallized microstructure with flat and elongated grains in the rolling plane of the plate. The alloy contains coherent precipitates, dispersoids of different sizes and large iron-based intermetallic inclusions [14]. In addition, the alloy has precipitate free zones at the nanoscale created during the artificial aging, and these zones are generally located around the grain boundaries. It is referred to Fourmeau et al. [56, 57] for a more detailed description of the experimental study of this alloy.

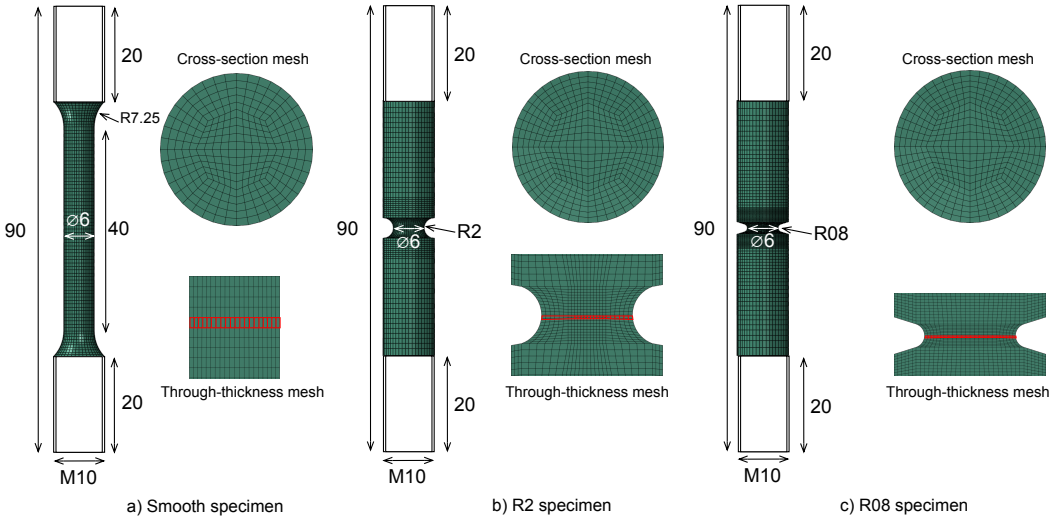

Figure 2: Overview of the specimens used in the experimental study: a) smooth specimen, b) R2 specimen (notch radius is 2 mm) and c) R08 specimen (notch radius is 0.8 mm). All measures are in mm. The finite element meshes used in the subsequent numerical simulations are also shown.

Axisymmetric tensile specimens were used to study the in-plane behaviour of the

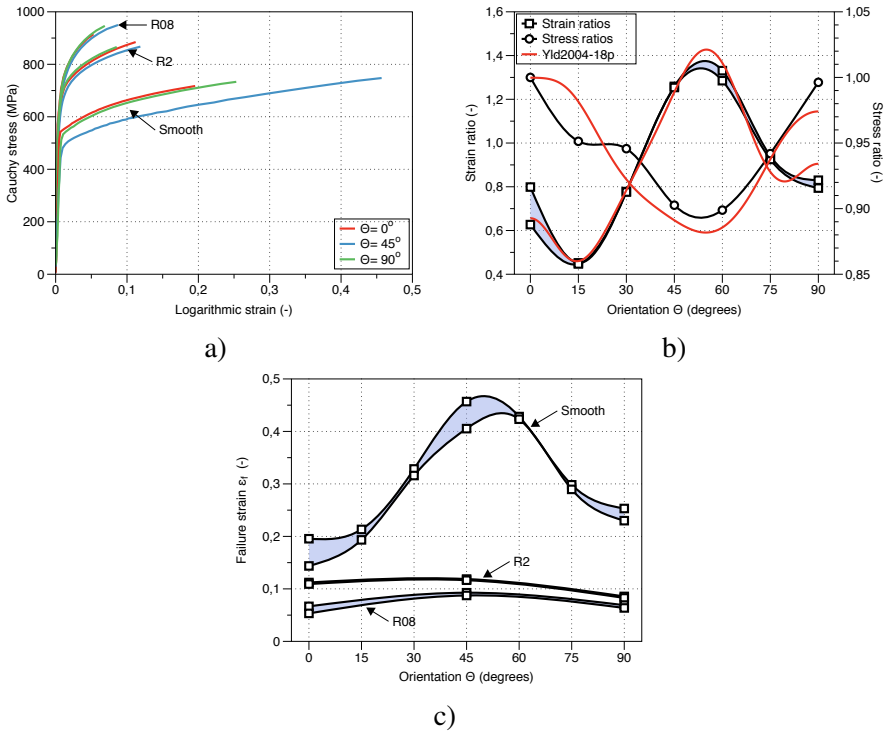

Figure 3: Summary of the experimental results: a) Cauchy stress-logarithmic strain curves for the smooth, 2 mm notch radius (R2) and 0.8 mm notch radius (R08) specimens carried out in the rolling direction ($\Theta = 0°$), transverse direction ($\Theta = 90°$) and at 45° from the rolling direction ($\Theta = 45°$), b) strain and stress ratios as function of the material orientation based on the experimental results and the Yld2004-18p yield surface [58] and c) failure strains for the smooth, 2 mm notch radius (R2) and 0.8 mm notch radius (R08) specimens as function of the material orientation with their scatter bands.

AA7075-T651 alloy. Smooth specimens were sampled in seven different orientations of the plate (0°, 15°, 30°, 45°, 60°, 75° and 90° with respect to the rolling direction (RD)) to reveal the anisotropic properties of the material, while notched specimens with two different notch root radii ($R = 2.0$ mm and $R = 0.8$ mm) were taken in three different directions of the plate (0°, 45° and 90° with respect to the rolling direction) to study the behaviour at increased stress triaxiality. The geometries of the tensile specimens are given in Figure 2. The tests were performed in a universal testing machine at room temperature and a nominal strain-rate of 5×10^{-4} s^{-1} (i.e., quasi-static loading conditions).

During testing, the force and the diameters of the minimum cross-section of the specimen were continuously measured until fracture. By assuming plastic incompressibility, the Cauchy stress σ and the logarithmic strain ε_l were calculated from the measured force F and current minimum cross-section area A as

$$\sigma = \frac{F}{A}, \quad \varepsilon_l = \ln\left(\frac{A_0}{A}\right) = \ln\left(\frac{D_0^2}{D_{ND}D_\perp}\right) \tag{1}$$

where $A_0 = \pi D_0^2/4$ and D_0 are the initial area and cross-section diameter of the specimen, respectively. The current elliptical cross-section area of the specimen was calculated as $A = \pi D_{ND} D_\perp/4$, where D_{ND} is the diameter in the normal direction of the plate (ND) and $D_\perp$ is the diameter in the transverse direction of the specimen.

Figure 3 a) shows representative curves from smooth and notched specimen tests in terms of Cauchy stress and logarithmic strain averaged over the minimum cross-section diameter for three directions (0°, 45° and 90°). The scatter between parallel tests was found to be negligible. A significant anisotropy in both the flow stress and strain to failure was exhibited, especially for the smooth specimen. Figure 3 b) gives strain and stress ratios (see [56] for definitions) as a function of loading direction for the smooth specimens. Again, significant variation with orientation was obtained. Finally, Figure 3 c) illustrates the variation in strain to failure with loading direction. It was noted that the anisotropy in strain to failure was in general related to the directional variation of the strain ratio. Thus, the lower the strain ratio, the lower was the strain to failure.

3. Anisotropic porous plasticity

3.1. Description of the model

The Gurson model [53] is used to induce strain softening in the strain localization analyses. In order to include anisotropic plasticity, the equivalent stress of the Gurson

model is defined by the Yld2004-18p yield function [58], whereas the other parts of the model remain unaltered. The credibility of this heuristic modification of the Gurson model has recently been studied by Dæhli et al. [35], and the agreement between the porous plasticity model and 3D unit cell analyses was found to be acceptable. A similar extension has previously been proposed and employed by Steglich et al. [33]. Several attempts have been made in the literature to derive rigourously an anisotropic porous plasticity model [30, 59, 60]. These models, while being able to describe anisotropic void growth and the complex interactions between the shape of the void and the anisotropy of the matrix material, are based on the orthotropic Hill yield criterion [61] for the matrix material. As the main focus of this study is placed on the effect of material anisotropy on ductile failure, the heuristic modification of the Gurson model [35] is preferred in order to get a better description of the matrix plastic anisotropy.

The model is formulated using the corotational stress approach. Thus, all tensor quantities are referred to a coordinate frame that rotates with the material axes. The corotational stress and rate-of-deformation tensors are then defined by $\hat{\boldsymbol{\sigma}} = \boldsymbol{R}^T \cdot \boldsymbol{\sigma} \cdot \boldsymbol{R}$ and $\hat{\boldsymbol{D}} = \boldsymbol{R}^T \cdot \boldsymbol{D} \cdot \boldsymbol{R}$, where $\boldsymbol{\sigma}$ and $\boldsymbol{D}$ are the Cauchy stress tensor and the rate-of-deformation tensor, respectively. The rotation tensor $\boldsymbol{R}$ is defined by the rate equation, $\dot{\boldsymbol{R}} = \boldsymbol{W} \cdot \boldsymbol{R}$, where $\boldsymbol{W}$ is the spin tensor. Possible changes in the plastic anisotropy due to texture evolution during deformation are neglected in this study.

The rate-of-deformation tensor $\hat{\boldsymbol{D}}$ is additively decomposed into elastic and plastic parts, so that

$$\hat{\boldsymbol{D}} = \hat{\boldsymbol{D}}^e + \hat{\boldsymbol{D}}^p \tag{2}$$

The corotational stress rate tensor is defined by the hypoelastic relation

$$\dot{\hat{\boldsymbol{\sigma}}} = \hat{\boldsymbol{C}} : \hat{\boldsymbol{D}}^e \tag{3}$$

where $\hat{\boldsymbol{C}}$ is the isotropic elasticity tensor defined in terms of Young's modulus E and Poisson's ratio ν. The Gurson yield function is given by

$$\Phi = \left(\frac{\sigma_{eq}\left(\hat{\boldsymbol{\sigma}}\right)}{\sigma_M}\right)^2 + 2q_1 f \cosh\left(\frac{q_2}{2}\frac{\hat{\boldsymbol{\sigma}} : \boldsymbol{I}}{\sigma_M}\right) - \left(1 + q_3 f^2\right) \tag{4}$$

where $\sigma_{eq}\left(\hat{\boldsymbol{\sigma}}\right)$ is the equivalent stress defined by the Yld2004-18p yield function, σ_M is the flow stress of the matrix, f is the porosity, q_1, q_2 and q_3 are parameters introduced by Tvergaard [54] and $\boldsymbol{I}$ is the second-order identity tensor. We refer to [56] and [58] for the definition of the equivalent stress of the Yld2004-18p yield function. Associative plastic flow is assumed and thus

$$\hat{\boldsymbol{D}}^p = \dot{\lambda}\frac{\partial \Phi}{\partial \hat{\boldsymbol{\sigma}}} \tag{5}$$

where $\dot{\lambda}$ is the plastic parameter, defined by the loading-unloading conditions in Kuhn-Tucker form

$$\Phi \leq 0,\ \dot{\lambda} \geq 0,\ \dot{\lambda}\Phi = 0 \tag{6}$$

The behaviour of the matrix material is given by

$$\sigma_M = \sigma_0 + Q\left(1 - \exp\left(-Cp\right)\right) \tag{7}$$

where σ_0 is the initial yield stress, Q and C are hardening parameters, and the equivalent plastic strain p is obtained as

$$p = \int \dot{p}\, dt = \int \frac{\hat{\boldsymbol{\sigma}} : \hat{\boldsymbol{D}}^p}{\left(1 - f\right)\sigma_M}\, dt \tag{8}$$

The evolution of the porosity is decomposed into growth and nucleation of voids, viz.

$$\dot{f} = \dot{f}_g + \dot{f}_n \tag{9}$$

The initial value of the porosity is denoted f_0. Based on matrix incompressibility, the void growth rate $\dot{f}_g$ is obtained by

$$\dot{f}_g = (1 - f)\,\hat{\boldsymbol{D}}^p : \boldsymbol{I} \tag{10}$$

Following [55], the void nucleation rate $\dot{f}_n$ is taken as

$$\dot{f}_n = \mathcal{A}\dot{p} \tag{11}$$

where

$$\mathcal{A} = \frac{f_n}{s_n\sqrt{2\pi}} \exp\left[-\frac{1}{2}\left(\frac{p - p_n}{s_n}\right)^2\right] \tag{12}$$

In this equation, f_n is the volume fraction of void nucleating particles, p_n is the mean equivalent plastic strain for nucleation, and s_n is the associated standard deviation.

3.2. Parameter identification

Two sets of material parameters are required in the porous plasticity model, the ones pertaining to the matrix material (anisotropic yield surface and isotropic work hardening) and the ones related to the porous behaviour (the parameters introduced by Tvergaard [54]). The initial void volume fraction f_0 and void nucleation parameters f_n, p_n and s_n, which are usually used as material parameters, are here restricted to the imperfection analyses and their identification is detailed later in the manuscript. The non-quadratic anisotropic yield function Yld2004-18p proposed by Barlat et al. [58] was calibrated using tensile tests in seven in-plane directions, an upsetting test (through-thickness compression test), and shear tests in three in-plane directions, assuming orthotropic symmetry (see Fourmeau et al. [56] for details). The initial yield stress σ_0 as well as the isotropic work-hardening parameters Q and C were calibrated using the tensile test in

the rolling direction. The list of material parameters is omitted in this article and the readers are referred to [56] for more details. The porous plasticity parameters q_1, q_2 and q_3 should, in principle, be calibrated for the given work-hardening rule and anisotropic yield surface, as done by Dæhli et al. [35], but are here given standard values from the literature ($q_1 = 1.5$, $q_2 = 1.0$ and $q_3 = q_1^2$).

4. Strain localization theory

Localization theory is used hereafter to exhibit the roles played by anisotropy in the failure process of the material. As proposed in Rice [38], an imperfection in the form of a planar band with slightly weaker material properties than the rest of the material, in which it is embedded, is considered. The presence of this imperfection allows strain localization to occur at reasonable strain levels [39]. This approach is used herein and is briefly recalled in this section, whereas for a detailed presentation of the method the readers are referred to [38, 45, 47].

The stress and strain rates as well as the constitutive relations inside the band are allowed to be different from those outside the band, with the requirement of equilibrium and compatibility across the band being enforced. The equation for continuing equilibrium is expressed as

$$\boldsymbol{n} \cdot \dot{\boldsymbol{P}}_b = \boldsymbol{n} \cdot \dot{\boldsymbol{P}} \tag{13}$$

where $\dot{\boldsymbol{P}}$ is the rate of the nominal stress tensor, $\boldsymbol{n}$ is the normal to the band in the current configuration and the subscript b denotes a quantity inside the band. The orientation of the imperfection band with respect to the global Cartesian coordinate system (X, Y, Z) is

defined by

$$\boldsymbol{n} = \left\{ \begin{array}{c} \cos\phi \\ \cos\theta \sin\phi \\ \sin\theta \sin\phi \end{array} \right\} \tag{14}$$

where ϕ is the angle between $\boldsymbol{n}$ and the X-axis, and θ is the angle between the Y-axis and the projection of $\boldsymbol{n}$ onto the YZ plane. For an anisotropic material, the critical orientation of the band $\boldsymbol{n}$ is found within the bounds $\phi \in [0, \pi]$ and $\theta \in [0, 2\pi]$. The orientation of the band relative to the global axes of a tension specimen is illustrated in Figure 4.

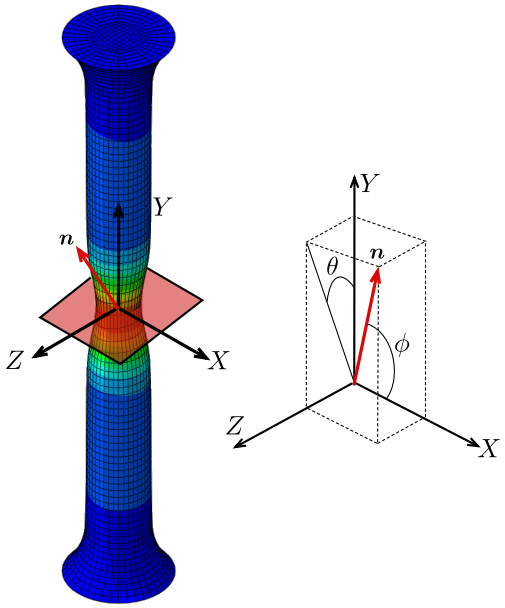

Figure 4: Definition of the band orientation relative to the global axes of the tension specimen.

Compatibility implies that the velocity gradient $\boldsymbol{L}_b$ inside the band takes the form [38]

$$\boldsymbol{L}_b = \boldsymbol{L} + \dot{\boldsymbol{q}} \otimes \boldsymbol{n} \tag{15}$$

where $\boldsymbol{L}$ is the velocity gradient of the material outside the band and $\dot{\boldsymbol{q}}$ is a vector that

represents the rate-of-deformation non-uniformity. The unit vector $\boldsymbol{m} = \dot{\boldsymbol{q}}/\|\dot{\boldsymbol{q}}\|$ determines the instantaneous character of the imperfection band. If $\boldsymbol{m} \cdot \boldsymbol{n} = 0$, the band has the character of a shear band, while if $\boldsymbol{m} \cdot \boldsymbol{n} = 1$, the band has the character of a dilatation band.

By combining Equations (13) and (15), an equation for the rate-of-deformation non-uniformity $\dot{\boldsymbol{q}}$ is obtained as

$$(\boldsymbol{n} \cdot \boldsymbol{C}_b^t \cdot \boldsymbol{n}) \cdot \dot{\boldsymbol{q}} = \boldsymbol{n} \cdot \left(\boldsymbol{C}^t - \boldsymbol{C}_b^t\right) : \boldsymbol{L} \tag{16}$$

where $\boldsymbol{C}^t$ and $\boldsymbol{C}_b^t$ are the tangent modulus tensors outside and inside the band, respectively (see Morin et al. [47] for details). Loss of ellipticity, or strain localization, occurs when the acoustic tensor of the band material, $\boldsymbol{A}_t(\boldsymbol{n}) = \boldsymbol{n} \cdot \boldsymbol{C}_b^t \cdot \boldsymbol{n}$, becomes singular, viz.

$$\det\left(\boldsymbol{n} \cdot \boldsymbol{C}_b^t \cdot \boldsymbol{n}\right) = 0 \tag{17}$$

For materials undergoing associative plastic flow, this condition is not met for reasonable stress levels unless strain softening is present in the constitutive response of the material in the imperfection band [38]. In this study, the anisotropic porous plasticity model with associative plastic flow described above is used inside the imperfection band, while the material outside the band is described using an anisotropic metal plasticity model obtained by restricting the initial void content f_0 and void nucleating particles f_n to be equal to zero.

The localization analysis by the imperfection band approach has been implemented numerically in a stand-alone FORTRAN programme, as described in detail by Morin et al. [47].

5. Numerical procedures

5.1. Finite element analyses

The finite element simulations of the smooth and notched tensile tests are carried out in ABAQUS/standard [62] using solid elements with reduced integration. An overview of the finite element meshes applied for the three specimens is given in Figure 2. These meshes are the same as those used in [56, 57] and the element length is approximately 0.3 mm. The porous plasticity model described in Section 3 is implemented in ABAQUS/Standard using a user-material subroutine (UMAT). When running the finite element simulations of the tension tests, the initial porosity f_0 and the volume fraction of void nucleating particles f_n are set to zero, thus reducing the anisotropic porous plasticity model to an anisotropic metal plasticity model with isochoric plastic flow.

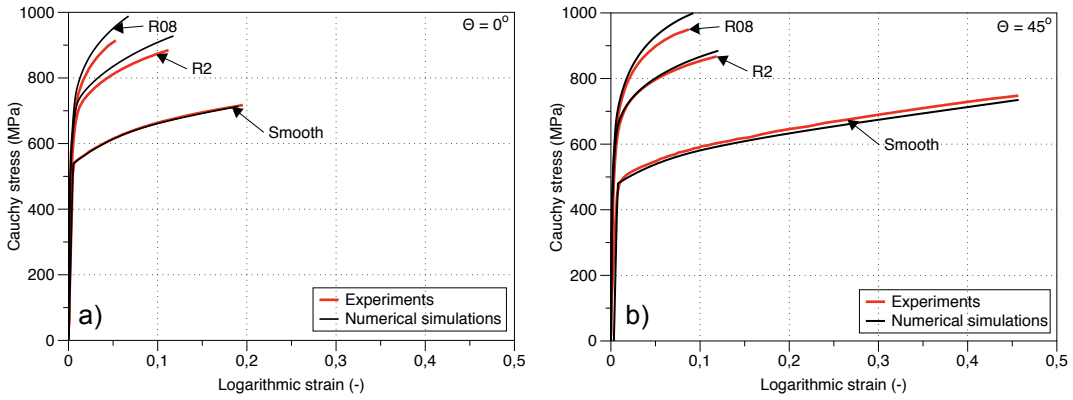

Figure 5: Experimental versus simulated stress-strain curves for the smooth and notched tensile tests: a) in the rolling direction and b) at 45° from the rolling direction.

Figure 5 presents the results from a selection of numerical simulations compared to the corresponding experiments. The smooth and notched specimens (with 2 mm radius and 0.8 mm radius) extracted from the rolling direction and at the 45° direction are used as examples to evaluate the accuracy of the chosen anisotropic metal plasticity model.

From Figure 5 a), it appears that a good correlation is obtained for the smooth tensile test in the rolling direction while the stress level is overestimated in the presence of a notch. When the specimens are oriented at 45° from the rolling direction (Figure 5 b)), the stress level is slightly underestimated in the smooth tensile tests as a result of the calibrated yield surface (Figure 3 b)) which underestimate the yield stress in this material orientation. The simulated notched specimens still exhibit a higher stress level than in the experiments but the discrepancy is somewhat reduced compared to the simulations in the rolling direction. In this study, the exponent of the Yld2004-18 yield surface [58] was fixed to 8, while Fourmeau et al. [56] showed that by increasing the exponent to 12 a better description of the stress level in the notched specimens could be obtained. Despite the discrepancies in the simulations of the notched tensile tests, the overall agreement between the numerical models and the experimental tests is found acceptable.

5.2. Localization analyses

The exact location of incipient ductile failure within the tensile specimens is not known, but it is reasonable to assume that failure initiates at the minimum cross-section. Accordingly, localization analyses are performed for all elements across the minimum cross-section, as defined in Figure 2. The numerical procedure is as follows (see also Figure 1):

1. The deformation gradient $\boldsymbol{F}(t)$ of each element within the minimum cross-section is calculated based on the nodal displacements and the isoparametric shape functions.
2. An imperfection analysis is run for each of these elements based on the extracted deformation gradient $\boldsymbol{F}(t)$ for a large number of band orientations defined by $\phi_0 \in [0, \pi]$ and $\theta_0 \in [0, 2\pi]$, using a domain reduction method as described in Morin et al. [47] which involves around 1200 bands.

3. For each element, a local failure strain p_f is calculated as the minimum equivalent plastic strain outside the band at loss of ellipticity inside the band for all band orientations.
4. The local failure strain p_f of each element is mapped onto the minimum cross-section of the specimen.
5. Using the relationship between the local equivalent plastic strain of the elements and the macroscopic logarithmic strain ε_l from the finite element simulation of the specimen, the macroscopic failure strain ε_f corresponding to localization within the actual element is mapped onto the minimum cross-section of the specimen.
6. The actual failure strain corresponds to the minimum value of ε_f over the minimum cross-section and its position is assumed to be the location of failure initiation.

The numerical procedure of finding the location of incipient failure and the macroscopic failure strain ε_f is illustrated in Figure 1. In the subsequent sections, the localization band is defined as the one for which loss of ellipticity occurs first, thus leading to the lowest macroscopic failure strain ε_f.

6. Numerical results

6.1. Calibration of the imperfection method

When running an imperfection analysis, the magnitude of the imperfection has to be calibrated. By applying void nucleation in the Gurson model inside the localization band, the calibration involves three parameters, namely the volume fraction of void nucleating particles f_n, the mean equivalent plastic strain for nucleation p_n, and the associated standard deviation s_n. The calibration of these three parameters requires the use of at least three different experimental tests, and here it is based on the smooth and

notched tests in the rolling direction of the material. The parameters of the void nucleation rule are identified based on a sensitivity analysis until a reasonable agreement with the experimental data is found.

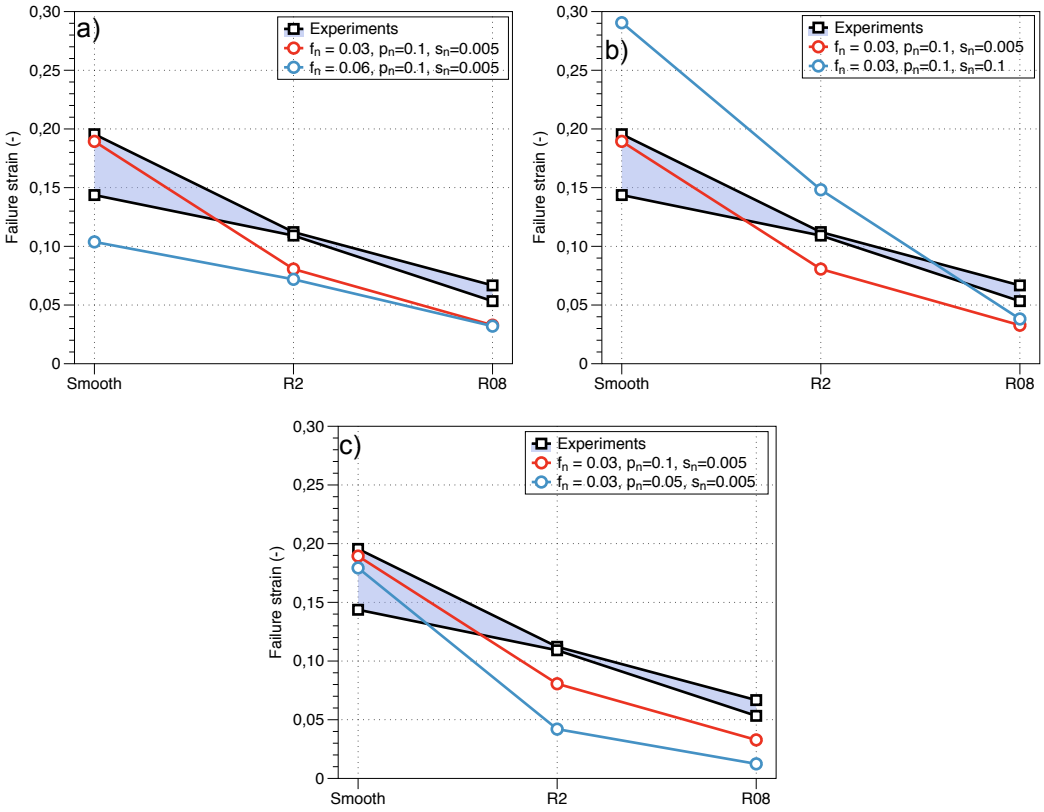

Figure 6: Calibration of the void nucleation parameters: a) effect of the volume fraction of void nucleating particles f_n, b) effect of the standard deviation s_n and c) effect of the mean equivalent plastic strain for nucleation p_n.

The effects of the different parameters involved in the void nucleation rule are presented in Figure 6. As shown in Figure 6 b), the standard deviation of the void nucleation rule s_n has a strong effect on the failure strain of the smooth and R2 specimens. In contrast, the amount of void nucleating at particles f_n (Figure 6 a)) has a rather strong effect for the smooth specimens but a limited impact for the R2 and R08 specimens. According

to Figure 6 c), the mean equivalent plastic strain p_n at nucleation has a small effect on the failure strain of the smooth sample, but is more important for the two notched samples. As the smooth specimens exhibit larger ductility, localization is more influenced by the amount of void nucleating particles (Figure 6 a)) rather than when the voids are nucleated (Figure 6 c)). In contrast, the R08 specimens are slightly more sensitive to p_n as they exhibit reduced ductility, and the failure predictions are therefore more sensitive to when voids starts to nucleate.

Based on the sensitivity analyses, the void nucleation parameters are taken as $f_n = 0.03$, $p_n = 0.1$ and $s_n = 0.005$. These parameters are applied in all remaining localization analyses of this study. It is worth noting that the obtained volume fraction of void nucleating particles f_n is within the range of observed particles content for this aluminium alloy [14].

An attempt was also made to model the imperfection based on a volume fraction of initial voids f_0 instead of a volume fraction of void nucleating particles f_n. To obtain the same ductility as when void nucleation is employed in the smooth tensile test, an initial void content f_0 of 2.7% was required. While there was no significant differences in the case of a smooth tensile test between the two voiding mechanisms, the failure prediction in the notched specimens was found to be overly conservative when a volume fraction of initial voids was applied. Therefore, all results presented in the next sections are based solely on void nucleating particles.

6.2. Details of an imperfection analysis

Before presenting the validation of the proposed approach it is important to detail the process leading to localization in an imperfection analysis. In this perspective, a selection of the important quantities driving an imperfection analysis are presented in Figure 7 for the case of the smooth tensile test in the rolling direction for the material outside

(black curves) and inside (red curves) the band. All quantities are plotted as a function of the logarithmic strain ε_l computed from the diameter reduction of the specimen.

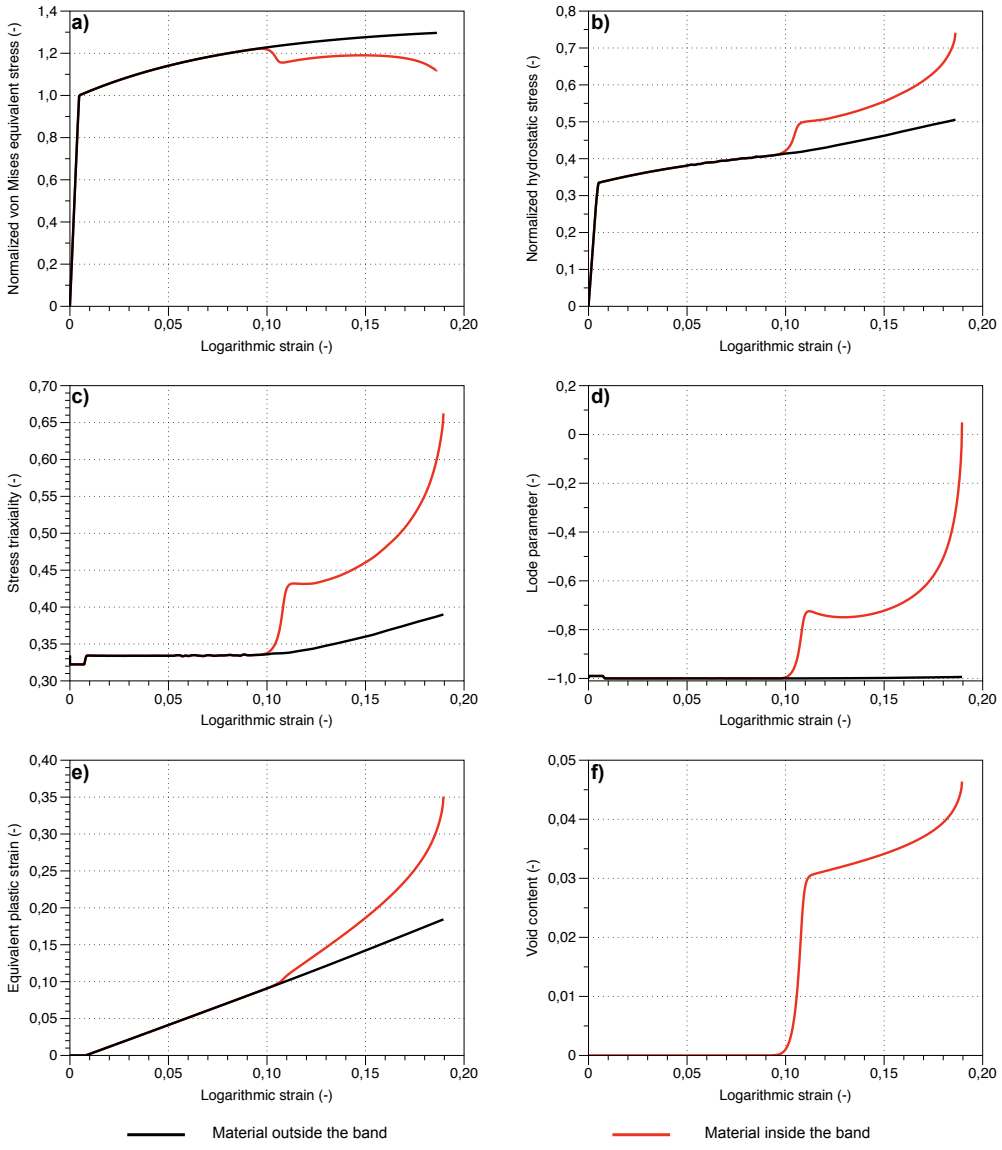

Figure 7: Evolution of important quantities outside and inside the localization band for a smooth tensile test in the rolling direction: a) the normalized von Mises equivalent stress, b) the normalized hydrostatic stress, c) the stress triaxiality, d) Lode parameter, e) the equivalent plastic strain and f) void content.

Figures 7 a) and b) present the von Mises equivalent stress σ_{vm} and hydrostatic stress $\sigma_h = \frac{1}{3}\boldsymbol{\sigma} : \boldsymbol{I}$ normalized with respect to the initial yield stress σ_0 in the rolling direction. Since the material inside the band is defined with void nucleation, the band does not have any initial porosity and exhibits the same von Mises equivalent stress and hydrostatic stress as the one outside the band (Figure 7 a) and b)) until the nucleation process takes place. At this point (Figure 7 f)), the stress state inside the band starts to drift both in terms of the stress triaxiality T (Figure 7 c)) and Lode parameter L (Figure 7 d)). The stress triaxiality T and the Lode parameter L are defined as

$$T = \frac{\sigma_h}{\sigma_{vm}}, \quad L = \frac{2\sigma_2 - \sigma_1 - \sigma_3}{\sigma_1 - \sigma_3} \tag{18}$$

where σ_1, σ_2 and σ_3 are the ordered principal stresses. The Lode parameter L equals -1 for generalized axisymmetric tension, 0 for generalized shear and $+1$ for generalized axisymmetric compression. It is interesting to note that the localization band exhibits strong variation in the stress triaxiality which is increasing compared to the value outside the band and that the Lode parameter L is drifting from generalized axisymmetric tension ($L = -1$) to generalized shear ($L = 0$), as also seen by Morin et al. [47]. As the void nucleation process proceeds, the imperfection starts to experience a higher equivalent plastic strain rate than the material outside the band until loss of ellipticity is reached (Figure 7 e)).

Even if the quantities of the localization band differ from those outside the band after the initiation of void nucleation, all stress quantities and equivalent plastic strains are related to the material outside the band in the remaining sections.

6.3. Assessment of the imperfection method

The identified imperfection model (i.e., the void nucleating localization band) is assessed against the experimental failure strains obtained with the smooth tensile tests and

notched tensile tests carried out in the remaining material orientations. Figure 8 shows the comparison between the experimental failure strains and the predictions based on the imperfection analyses. The reported failure strains (from the localization analyses) correspond to the time when loss of ellipticity is detected in one element. An overall good agreement is found for the smooth tensile tests, while the predicted failure strains are conservative for the tests carried out at 45° and 60° from the rolling direction. Even if the imperfection band approach is applied here to predict failure, this methodology should in fact be conservative as localization is preceding ductile failure. Moreover, the tests carried out at 45° and 60° from the rolling direction exhibit a significantly larger ductility than the one in the rolling direction. Under such deformations, the shape of the voids, induced by the deformation of the matrix material, might become important and should perhaps be considered in the anisotropic porous plasticity model, as done by Keralavarma and Benzerga [59], Keralavarma et al. [23] and Morin et al. [60]. Nevertheless, the proposed methodology appears capable of predicting anisotropic failure in view of the results from the smooth tensile tests.

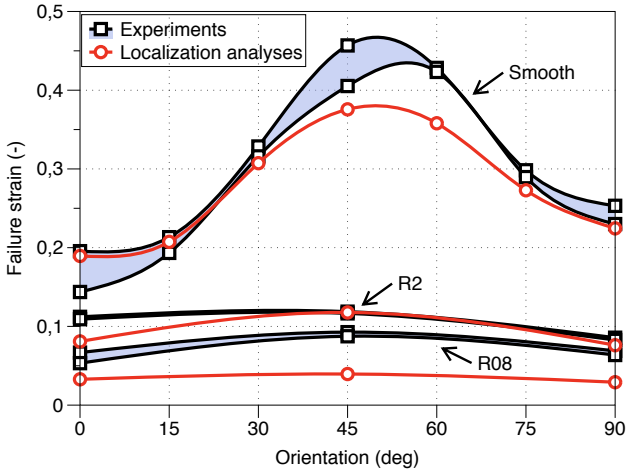

Figure 8: Failure strains obtained with imperfection analyses compared with the experimental measurements for the smooth and notched specimens.

Figure 9 presents the failure strains predicted by the localization analyses in each element of the minimum cross-section of the smooth specimens. The initiation of ductile failure is usually assumed to occur in the centre of a tensile test specimen [63]. In the present analyses, loss of ellipticity is always reached in the centre of the smooth specimen independently of the orientation of the specimen which seems in line with observations from the literature. For each of the specimen orientations illustrated in Figure 9, the magnitude of the predicted failure strains is indicated by black and white colourbars. As the overall ductility is increasing, necking becomes more pronounced and a larger spread appears in the failure strains. For the lowest ductility, reached in the rolling direction, the maximum predicted failure strain in the cross-section is close to 0.25 while the minimum is close to 0.19. Thus, the failure strain field appears rather smooth. In the case of the largest ductility, obtained at 45° of the rolling direction, the maximum predicted failure strain is close to 0.65 while the minimum is close to 0.37. As necking has more time to develop in this specimen, the failure strain field map is more heterogeneous and the difference between the minimum and maximum failure strain is larger. The orientation of the localization band, though difficult to relate to the failure plane of the tensile tests, shows some interesting features. When loss of ellipticity is predicted in the rolling direction, the localization band contains the transverse direction as shown by Børvik et al. [64] and form an angle of approximately 45° to the loading axis. The localization bands of the remaining material orientations do not contain any specific material axes as shown by Fourmeau et al. [57] and form an angle in between 32° and 39° to the loading axis, with the minimum being in the 45° tensile test. By looking at the complementary angle α, defined as $\cos\alpha = \boldsymbol{m} \cdot \boldsymbol{n}$, the deformation mode of the localization band can be interpreted. When the complementary angle α is equal to 90° the localization band experiences a shear deformation mode, while $\alpha = 0°$ implies a dilatation mode. In the smooth tensile test, the complementary angle α varies from 86°

to 84° at loss-of-ellipticity with its maximum in the tensile tests carried out in the rolling and transverse directions and its minimum in the test carried out at 45° to the rolling direction. This indicates that the localization bands are subjected to a shear-dominated deformation mode.

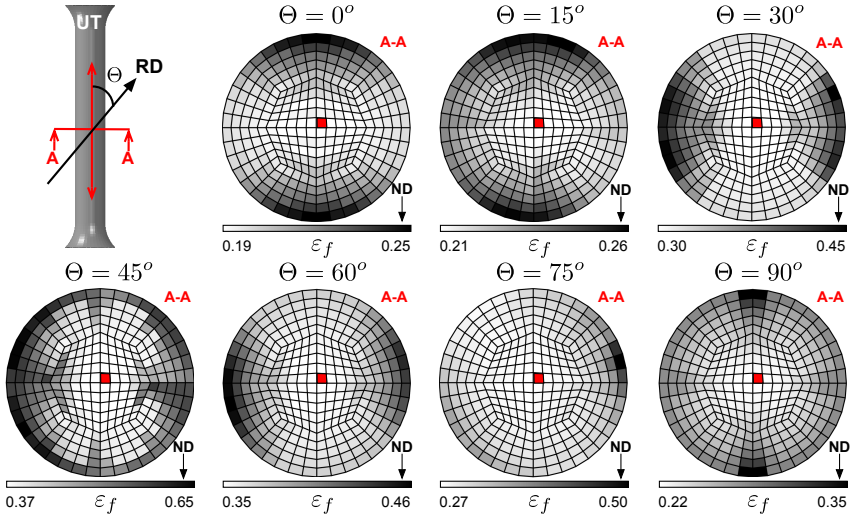

Figure 9: Failure strain maps on the minimum cross section obtained with the localization analyses as function of the material orientation for the smooth specimens. The location of failure initiation is indicated by the red elements.

The failure strains predicted for the notched specimens with a 2 mm radius (see also Figure 8) exhibit a lower failure strain in the rolling direction compared to the experiments, while the magnitude of the failure strains for the specimens at 45° and 90° to the rolling direction are rather reasonable. Due to the presence of a notch, the strain and stress states across the specimen become more heterogeneous [57]. These heterogeneities combined with the anisotropic behaviour of the investigated aluminium alloy lead to different locations for the initiation of ductile failure, indicated by the red elements in Figure 10. Accordingly, the field map of the failure strains exhibits rather different patterns depending of the orientation of the specimen. For instance, ductile failure

initiates in the root of the notch for the specimens in the rolling direction ($\Theta = 0°$) and transverse direction ($\Theta = 90°$), while it is almost mid-way from the center of the specimen to the root of the notch for the specimen oriented at 45° to the rolling direction, see Figures 10 a), c) and b) respectively. These results indicate a strong interplay between the anisotropic behaviour of the material and the geometry of the specimen.

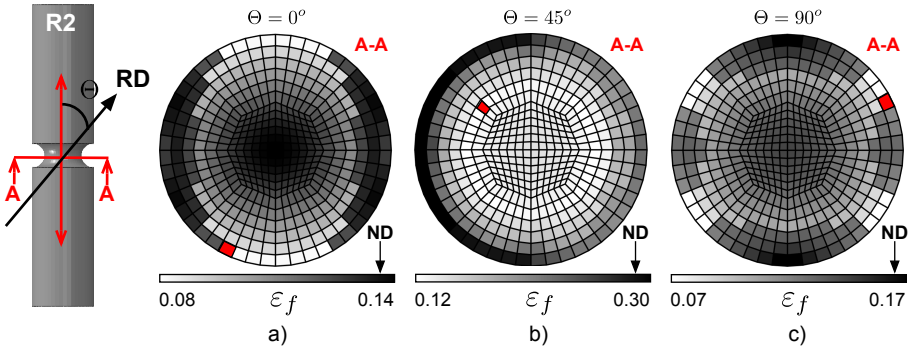

Figure 10: Failure strain maps on the minimum cross section obtained with the localization analyses for the notched specimens with a radius of 2 mm at: a) 0°, b) 45° and c) 90° with respect to the rolling direction. The location of failure initiation is indicated by the red elements.

From Figure 8, it appears that the predicted failure strains for the notched specimens with a radius of 0.8 mm exhibit negligible anisotropy compared to the experiments. Moreover, the magnitude of the predicted failure strains is quite conservative compared with the experimental results. It is believed that the main reason behind the underestimated failure strain is the parameters employed in the void nucleation rule. The obtained parameters are based on a trade-off solution which allows a better description of the failure strains obtained in the rolling direction for the smooth and the 2 mm radius notched specimen, but underestimate the ductility for the specimens with the sharpest notch (see Figure 6). Moreover, the use of a void free material outside the imperfection band might be a rather strong assumption in the case of the 0.8 mm radius notch specimens. In these experiments, a damage mechanism taking place outside the imperfection band could

have a stronger impact on the results as the stress triaxiality is high. Another potential explanation for the underestimation of the ductility might be related to the higher stress level predicted in the numerical simulations compared to the experiments (Figure 5). As stated earlier, increasing the exponent of the Yld2004-18p [58] from 8 to 12 reduces the stress level in the numerical analyses [57]. This effect was evaluated in the present study by re-running all analyses with this higher exponent, but no significant improvements were observed. While increasing the exponent of the Yld2004-18p yield surface helps to better capture the stress level of the experiments, it increases at the same time the curvature of the yield surface and this might trigger localization earlier. This effect was observed by Dæhli et al. [52] where localization analyses were run, in a similar setup as in the present study, for a von Mises and a Hershey/Hosford yield surface [65, 66]. Despite the mismatch in the magnitude of the failure strain it is interesting to look at the location of failure initiation (Figure 11). While the notched specimen with a radius of 2 mm exhibits large differences in the location of failure initiation and in the failure strain field map (Figure 10), a notch with 0.8 mm radius appears to initiate failure in the root of the notch even though it is not initiated at the same location (Figure 11).

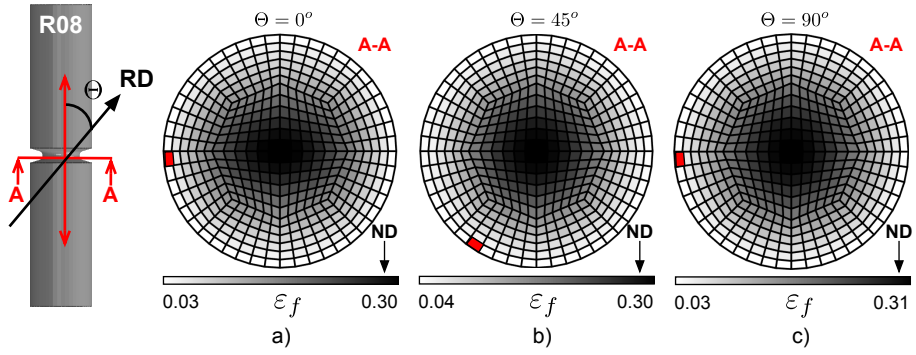

Figure 11: Failure strain maps on the minimum cross section obtained with the localization analyses for the notched specimens with a radius of 0.8 mm at: a) 0°, b) 45° and 90° with respect to the rolling direction. The location of failure initiation is indicated by the red elements.

In the case of the notched specimens, the localization bands do not show any preferred orientation and do not include any specific material axes. The localization bands form an angle of about 37°, while the complementary angle α is slightly smaller than the ones found for the smooth specimens. This indicates that the localization bands still exhibit a shear-dominated deformation mode in the range of investigated stress triaxialities. As indicated by Morin et al. [47], an imperfection band based on void nucleation would exhibit a shear-dominated deformation mode even at large stress triaxialities.

6.4. Analysis of the simulation results

In this section, we present an analysis of the simulation results obtained in an attempt to identify the sources for the predicted anisotropy in tensile ductility. To this end, two stress quantities are extracted from the material outside the localization band in the critical element (i.e., the element where localization occurs first). These are the von Mises equivalent stress σ_{vm} and the hydrostatic stress σ_h which are normalized with respect to the initial yield stress σ_0 of the material in the rolling direction. Additionally, the equivalent plastic strain p developed outside the localization band as well the void content f of the localization band are extracted. It should be recalled that the localization band orientation is defined here as the orientation first experiencing loss of ellipticity among all orientations in the critical element. All these quantities are plotted as function of the logarithmic strain ε_l obtained from the diameter reduction of the specimens.

Figure 12 shows the said quantities extracted from the smooth tensile specimens in the rolling direction ($\Theta = 0°$), transverse direction ($\Theta = 90°$) and at 45° with respect to the rolling direction ($\Theta = 45°$). When changing the orientation of the specimen with respect to the rolling direction, the yield stress changes and leads to different stress levels inside the specimens (Figure 12 a)). Due to the lower stress ratio at 45° to the rolling direction (see Figure 3 b)), the magnitude of the stress is lowered and as a result the

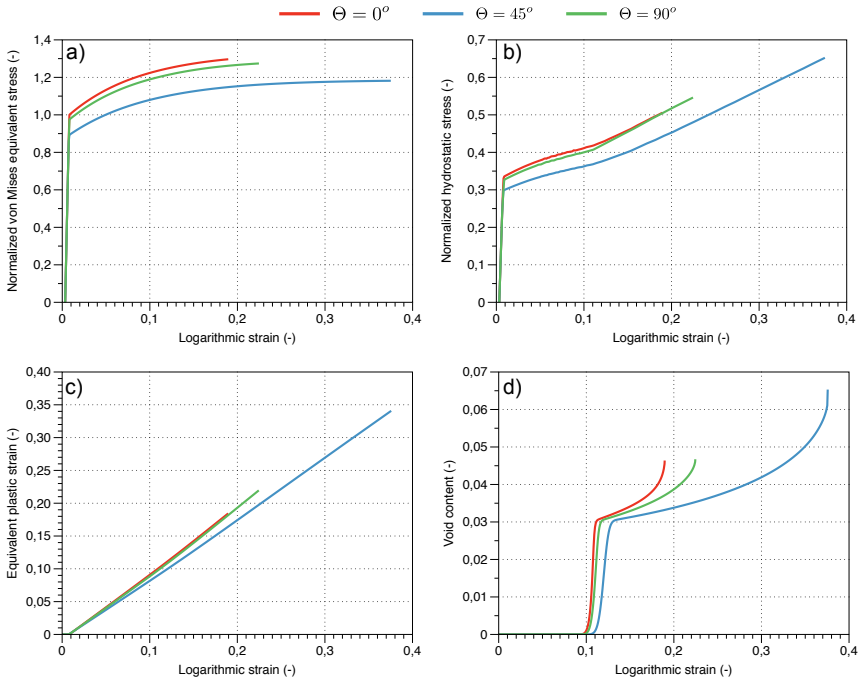

Figure 12: Evolutions as function of the logarithmic strain ε_l of: a) the normalized von Mises equivalent stress, b) the normalized hydrostatic stress, c) the equivalent plastic strain outside the localization bands and d) the void content inside the localization bands for the smooth tensile tests carried out at 0°, 45° and 90° to the rolling direction.

hydrostatic stress is the lowest for this material orientation (Figure 12 b)). For the same reason, a lower yield stress is found in the transverse direction (Θ = 90°) compared to the rolling direction (Figure 12 a)) and the resulting hydrostatic stress outside the band is therefore slightly reduced in the tensile test carried out in the transverse direction (Figure 12 b)). Figure 12 c) shows the evolution of the equivalent plastic strain at the location of failure initiation as a function of the logarithmic strain. Only small differences are present between the specimens at 0° and 90° to the rolling direction, while the specimen oriented at 45° exhibits a somewhat slower evolution of the equivalent plastic strain. While the different stress levels are related to the anisotropic yielding of the material, the local evolutions of the equivalent plastic strain can be related to the anisotropic plastic

flow through the strain ratios. The applied aluminium alloy has a low strain ratio in the rolling direction ($R_0 \approx 0.6$), a larger in the transverse direction ($R_{90} \approx 0.9$), and an even larger at 45° from the rolling direction ($R_{45} \approx 1.3$) (Figure 3 b)). The strong interaction between the geometrical constraint of the neck and the anisotropic plastic flow triggers different evolutions of the equivalent plastic strain depending on the orientation of the specimens. When combining the stress level with the development of the equivalent plastic strain in the center of the specimen, the localization bands, in which plastic strain driven void nucleation is present, display different void evolutions (Figure 12 d)). The void nucleation appears to be delayed at 45° from the rolling direction compared to the transverse and rolling directions. When the void nucleation process is completed, the effect of the stress level becomes very important and the void growth becomes much slower for the test oriented at 45° from the rolling direction due to the reduced yield stress. The differences in hydrostatic stress, i.e., the driving force of void growth, appear to be a key factor in the observed anisotropic failure. Based on Figure 12 d), the evolution of the porosity is rather strong from a macroscopic point of view, in particular near localization. With the relatively large amount of void nucleating particles present inside the band, significant void growth is obtained despite the low stress triaxiality of these experiments. The evolution in Figure 12 d) suggests that a coalescence criterion, as proposed by Pardoen and Hutchinson [67], Keralavarma and Chockalingam [68] or Torki et al. [69], may not be required in the present analyses.

Figure 13 shows the same quantities for the notched specimens with 2 mm radius. In contrast to the smooth tensile tests (Figure 9), the notched specimens with 2 mm radius exhibit different locations for failure initiation (Figure 10) which interacts with the plastic anisotropy of the material. For instance, the von Mises equivalent stresses (Figure 13 a)) developed at the location of failure initiation exhibit the same trends as for the smooth specimen (Figure 12 a)), but the resulting hydrostatic stresses are quite different

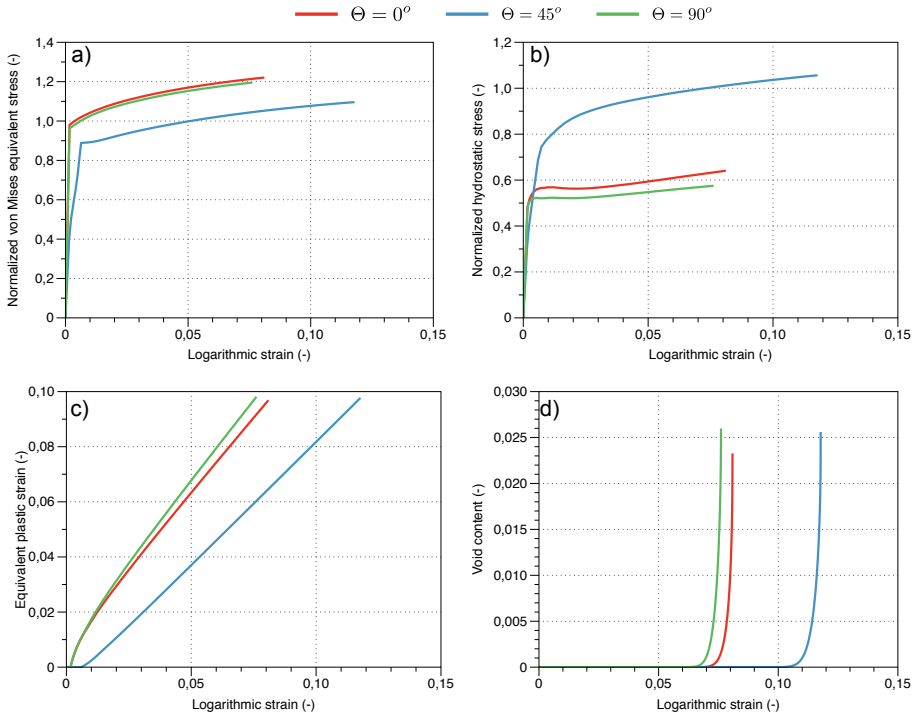

Figure 13: Evolutions as function of the logarithmic strain ε_l of: a) the normalized von Mises equivalent stress, b) the normalized hydrostatic stress, c) the equivalent plastic strain outside the localization bands and d) the void content inside the localization bands for the notched tensile tests with notch radius of 2 mm carried out at 0°, 45° and 90° to the rolling direction.

(Figure 13 b)). This effect is linked to the location of failure initiation and the different stress triaxialities resulting from the heterogeneities introduced by the notch. According to the analyses of the smooth tensile tests, a higher hydrostatic stress should lead to a lower ductility since void growth is very sensitive to this quantity, but the results obtained for the 2 mm radius notched specimen show otherwise. The reason for this difference is linked to the local evolution of the equivalent plastic strain as shown in Figure 13 c). Due to a combined effect of the anisotropic plastic flow and the location of failure initiation, a complex stress redistribution takes place in the specimen oriented at 45° from the rolling direction which slows down the evolution of the local equivalent plastic strain. As a

result of the spread of plasticity in the specimen, void nucleation is delayed (Figure 13 d)) in the 45° specimen compared to the ones in the rolling and transverse directions. The opposite occurs in the specimen oriented in the transverse direction compared to the rolling direction. Both the equivalent and hydrostatic stresses developed in the specimen in the transverse direction are slightly lower than in the rolling direction. Again based on the analyses carried out on the smooth specimen, the ductility of the specimen in the transverse direction should be higher than the one in the rolling direction, but the results indicate the opposite. Due to the stress redistribution, the specimen oriented in the transverse direction exhibits a slightly faster evolution of the equivalent plastic strain at the location of failure initiation (Figure 13 c)). This difference is enough to trigger the void nucleation sooner than in the specimen in the rolling direction and thus localization is reached earlier.

Similar analyses can be carried out for the notched specimen with radius of 0.8 mm but are not shown here for brevity.

Concluding remarks

The anisotropic failure of the aluminium alloy AA7075-T651 is investigated in this study. To this end, strain localization analyses employing the imperfection approach are used in an attempt to predict and understand anisotropic ductile failure. Smooth and notched tension tests, previously carried out on this alloy [57], are simulated with an anisotropic metal plasticity model. The local evolutions of the deformation gradient extracted from the critical cross-section of these specimens are then used in a series of imperfection analyses. The imperfection bands are modelled with an anisotropic porous plasticity model [35] in order to introduce strain softening and trigger loss of ellipticity. The proposed simulation approach, based on a homogeneized microstructure, is able to predict the observed anisotropic ductile failure in the plane of the rolled plate (without

details of the material's microstructure). The anisotropic failure observed in the smooth specimens is well predicted, from a qualitative point of view, and in most of the material orientation quantitatively as well. The prediction of failure initiation in the notched specimens is rather correct qualitatively, while a conservative estimate of the ductility is obtained for the specimens with the sharpest notch. While it is difficult to study the effect of plastic anisotropy on ductile failure experimentally, the proposed numerical approach provides a simple way to carry out such studies. Based on the present analyses, anisotropic ductile failure appears as a complex problem influenced by the stress level and the redistribution of stresses which are combined effects of the anisotropy of the alloy and the specimen's geometry.

While the proposed numerical approach provides reasonable agreement with the available experiments, there are other sources of anisotropic tensile ductility than plastic anisotropy. Morphological anisotropy due to the flat, elongated grains, the distribution of primary particles and the precipitate free zones along the grain boundaries can also contribute to the anisotropic tensile ductility but will not be captured with the current description of the material inside the imperfection band. However, a model including these effects, when available, is easily introduced in the imperfection band analysis.

Acknowledgements

The authors gratefully appreciate the financial support from NTNU and the Research Council of Norway through the Centre for Advanced Structural Analysis, Project No. 237885 (CASA) and the FRINATEK Programme, Project No. 250553 (FractAl). Part of this work was performed when A.B. was a visiting professor of the Structural Impact Laboratory at the Department of Structural Engineering, NTNU. A.B. also gratefully acknowledges the FractAl project for the financial support during his stay in Trondheim.

References

[1] K. Zhang, B. Holmedal, O. S. Hopperstad, S. Dumoulin, J. Gawad, A. Van Bael, and P. Van Houtte, "Multi-level modelling of mechanical anisotropy of commercial pure aluminium plate: Crystal plasticity models, advanced yield functions and parameter identification," *International Journal of Plasticity*, vol. 66, pp. 3–30, 2015.

[2] M. Khadyko, S. Dumoulin, G. Cailletaud, and O. S. Hopperstad, "Latent hardening and plastic anisotropy evolution in AA6060 aluminium alloy," *International Journal of Plasticity*, vol. 76, pp. 51–74, 2016.

[3] H. Zhang, M. Diehl, F. Roters, and D. Raabe, "A virtual laboratory using high resolution crystal plasticity simulations to determine the initial yield surface for sheet metal forming operations," *International Journal of Plasticity*, vol. 80, pp. 111–138, 2016.

[4] A. P. Karafillis and M. C. Boyce, "A general anisotropic yield criterion using bounds and a transformation weighting tensor," *Journal of the Mechanics and Physics of Solids*, vol. 41, no. 12, pp. 1859–1886, 1993.

[5] F. Bron and J. Besson, "A yield function for anisotropic materials Application to aluminum alloys," *International Journal of Plasticity*, vol. 20, no. 4-5, pp. 937–963, 2004.

[6] F. Barlat, J. W. Yoon, and O. Cazacu, "On linear transformations of stress tensors for the description of plastic anisotropy," *International Journal of Plasticity*, vol. 23, no. 5, pp. 876–896, 2007.

[7] D. J. Lloyd, "The scaling of the tensile ductile fracture strain with yield strength in Al alloys," *Scripta Materialia*, vol. 48, no. 4, pp. 341–344, 2003.

[8] G. Liu, S. Scudino, R. Li, U. Kühn, J. Sun, and J. Eckert, "Coupling effect of primary voids and secondary voids on the ductile fracture of heat-treatable aluminum alloys," *Mechanics of Materials*, vol. 43, no. 10, pp. 556–566, 2011.

[9] I. Westermann, K. O. Pedersen, T. Furu, T. Børvik, and O. S. Hopperstad, "Effects of particles and solutes on strength, work-hardening and ductile fracture of aluminium alloys," *Mechanics of Materials*, vol. 79, pp. 58–72, 2014.

[10] L. E. Bryhni Dæhli, T. Børvik, and O. S. Hopperstad, "Influence of loading path on ductile fracture of tensile specimens made from aluminium alloys," *International Journal of Solids and Structures*, vol. 88-89, pp. 17–34, 2016.

[11] A. Benzerga and J.-B. Leblond, "Ductile Fracture by Void Growth to Coalescence, in: Advances in Applied Mechanics," *Advances in Applied Mechanics*, vol. 10, pp. 169–305, 2010.

[12] M. Dunand and D. Mohr, "Effect of Lode parameter on plastic flow localization after proportional loading at low stress triaxialities," *Journal of the Mechanics and Physics of Solids*, vol. 66, no. 1, pp. 133–153, 2014.

[13] D. Steglich, W. Brocks, J. Heerens, and T. Pardoen, "Anisotropic ductile fracture of Al 2024 alloys," *Engineering Fracture Mechanics*, vol. 75, no. 12, pp. 3692–3706, 2008.

[14] J. B. Jordon, M. F. Horstemeyer, K. Solanki, J. D. Bernard, J. T. Berry, and T. N. Williams, "Damage characterization and modeling of a 7075-T651 aluminum plate," *Materials Science and Engineering A*, vol. 527, no. 1-2, pp. 169–178, 2009.

[15] I. Westermann, K. E. Snilsberg, Z. Sharifi, O. S. Hopperstad, K. Marthinsen, and B. Holmedal, "Three-point bending of heat-treatable aluminum alloys: Influence of microstructure and texture on bendability and fracture behavior," *Metallurgical and Materials Transactions A: Physical Metallurgy and Materials Science*, vol. 42, no. 11, pp. 3386–3398, 2011.

[16] D. Dumont, A. Deschamps, and Y. Brechet, "On the relationship between microstructure, strength and toughness in AA7050 aluminum alloy," *Materials Science and Engineering A*, vol. 356, no. 1-2, pp. 326–336, 2003.

[17] D. Dumont, A. Deschamps, and Y. Brechet, "A model for predicting fracture mode and toughness in 7000 series aluminium alloys," *Acta Materialia*, vol. 52, no. 9, pp. 2529–2540, 2004.

[18] M. Fourmeau, C. Marioara, T. Børvik, a. Benallal, and O. Hopperstad, "A study of the influence of precipitate-free zones on the strain localization and failure of the aluminium alloy AA7075-T651," *Philosophical Magazine*, vol. 6435, no. October, pp. 1–27, 2015.

[19] Y. Bao and T. Wierzbicki, "On fracture locus in the equivalent strain and stress triaxiality space," *International Journal of Mechanical Sciences*, vol. 46, no. 1, pp. 81–98, 2004.

[20] I. Barsoum and J. Faleskog, "Rupture mechanisms in combined tension and shear-Experiments," *International Journal of Solids and Structures*, vol. 44, pp. 1768–1786, 2007.

[21] H. Li, M. Fu, J. Lu, and H. Yang, "Ductile fracture: Experiments and computations," *International Journal of Plasticity*, vol. 27, pp. 147–180, feb 2011.

[22] G. Gruben, O. S. Hopperstad, and T. Borvik, "Evaluation of uncoupled ductile fracture criteria for the dual-phase steel Docol 600DL," *International Journal of Mechanical Sciences*, vol. 62, no. 1, pp. 133–146, 2012.

[23] S. M. Keralavarma, S. Hoelscher, and A. A. Benzerga, "Void growth and coalescence in anisotropic plastic solids," *International Journal of Solids and Structures*, vol. 48, no. 11-12, pp. 1696–1710,

2011.

[24] F. Scheyvaerts, P. R. Onck, C. Tekolu, and T. Pardoen, "The growth and coalescence of ellipsoidal voids in plane strain under combined shear and tension," *Journal of the Mechanics and Physics of Solids*, vol. 59, no. 2, pp. 373–397, 2011.

[25] C. Tekoglu, J. B. Leblond, and T. Pardoen, "A criterion for the onset of void coalescence under combined tension and shear," *Journal of the Mechanics and Physics of Solids*, vol. 60, no. 7, pp. 1363–1381, 2012.

[26] Z. G. Liu, W. H. Wong, and T. F. Guo, "Void behaviors from low to high triaxialities : Transition from void collapse to void coalescence," *International Journal of Plasticity*, vol. 84, pp. 183–202, 2016.

[27] I. Barsoum and J. Faleskog, "Rupture mechanisms in combined tension and shear Micromechanics," vol. 44, pp. 5481–5498, 2007.

[28] I. Barsoum and J. Faleskog, "Micromechanical analysis on the influence of the Lode parameter on void growth and coalescence," *International Journal of Solids and Structures*, vol. 48, no. 6, pp. 925–938, 2011.

[29] C. Tekolu, J. W. Hutchinson, and T. Pardoen, "On localization and void coalescence as a precursor to ductile fracture.," *Philosophical transactions. Series A, Mathematical, physical, and engineering sciences*, vol. 373, no. 2038, 2015.

[30] A. A. Benzerga and J. Besson, "Plastic potentials for anisotropic porous solids," *European Journal of Mechanics, A/Solids*, vol. 20, no. 3, pp. 397–434, 2001.

[31] W. Y. Chien, J. Pan, and S. C. Tang, "Modified Anisotropic Gurson Yield Criterion for Porous Ductile Sheet Metals," *Journal of Engineering Materials and Technology*, vol. 123, no. 4, p. 409, 2001.

[32] D. A. Wang, J. Pan, and S. D. Liu, "An Anisotropic Gurson Yield Criterion for Porous Ductile Sheet Metals with Planar Anisotropy," *International Journal of Damage Mechanics*, vol. 13, no. 1, pp. 7–33, 2004.

[33] D. Steglich, H. Wafai, and J. Besson, "Interaction between anisotropic plastic deformation and damage evolution in Al 2198 sheet metal," *Engineering Fracture Mechanics*, vol. 77, no. 17, pp. 3501–3518, 2010.

[34] S. M. Keralavarma and A. A. Benzerga, "Numerical assessment of an anisotropic porous metal plasticity model," *Mechanics of Materials*, vol. 90, pp. 212–228, 2015.

[35] L. E. B. Dæhli, J. Faleskog, T. Børvik, and O. S. Hopperstad, "Unit cell simulations and porous plasticity modelling for recrystallization textures in aluminium alloys," *Procedia Structural Integrity*,

vol. 2, pp. 2535—-2542, 2016.

[36] Z. Marciniak and K. Kuczyński, "Limit strains in the processes of stretch-forming sheet metal," *International Journal of Mechanical Sciences*, vol. 9, no. 9, pp. 609–620, 1967.

[37] J. W. Rudnicki and J. R. Rice, "Conditions for the localization of deformation in pressure-sensitive dilatant materials," *Journal of the Mechanics and Physics of Solids*, vol. 23, no. 6, pp. 371–394, 1975.

[38] J. R. Rice, "The localization of plastic deformation," in *14th International Congress of Theoretical and Applied Mechanics*, pp. 207–220, 1976.

[39] H. Yamamoto, "Conditions for shear localization in the ductile fracture of void-containing materials," *International Journal of Fracture*, vol. 14, no. 4, pp. 347–365, 1978.

[40] A. Needleman and J. R. Rice, "Limits to ductility set by plastic flow localization," 1979.

[41] M. Saje, J. Pan, and A. Needleman, "Void nucleation effects on shear localization in porous plastic solids," *International Journal of Fracture*, vol. 19, no. 3, pp. 163–182, 1982.

[42] J. Pan, M. Saje, and A. Needleman, "Localization of deformation in rate sensitive porous plastic solids," *International Journal of Fracture*, vol. 21, no. 4, pp. 261–278, 1983.

[43] M. Mear and J. Hutchinson, "Influence of yield surface curvature on flow localization in dilatant plasticity," *Mechanics of Materials*, vol. 4, pp. 395–407, dec 1985.

[44] A. Needleman and V. Tvergaard, "Analyses of Plastic Flow Localization in Metals," *Applied Mechanics Reviews*, vol. 45, no. 3, 1992.

[45] K. Nahshon and J. W. Hutchinson, "Modification of the Gurson Model for shear failure," *European Journal of Mechanics, A/Solids*, vol. 27, no. 1, pp. 1–17, 2008.

[46] G. Gruben, D. Morin, M. Langseth, and O. S. Hopperstad, "Strain localization and ductile fracture in advanced high-strength steel sheets," *European Journal of Mechanics, A/Solids*, vol. 61, pp. 315–329, 2017.

[47] D. Morin, O. S. Hopperstad, and A. Benallal, "On the description of ductile fracture in metals by the strain localization theory," *International Journal of Fracture*, Jul 2017.

[48] W. T. Koiter, *The stability of elastic equilibrium*. PhD thesis, Techische Hooge School, 1945.

[49] W. T. Koiter, "The effect of axisymmetric imperfections on the buckling of cylindrical shells under axial compression," *Prc Koninkl. Nederl Akademie van Wetenschappen*, vol. 66, no. B, pp. 265–279, 1963.

[50] B. Budiansky and J. W. Hutchinson, "Dynamic buckling of imperfection-sensitive structures," 1964.

[51] J. Hutchinson, "Imperfection-sensitivity in the plastic range," *Journal of the Mechanics and Physics*

of Solids, vol. 21, pp. 191–204, may 1973.

[52] L. E. B. Dæhli, D. Morin, T. Børvik, and O. S. Hopperstad, "Influence of yield surface curvature on the macroscopic yielding and ductile failure of isotropic porous plastic materials," *Journal of the Mechanics and Physics of Solids*, vol. 107, pp. 253–283, oct 2017.

[53] A. L. Gurson, "Continuum Theory of Ductile Rupture by Void Nucleation and Growth: Part I Yield Criteria and Flow Rules for Porous Ductile Media," *Journal of Engineering Materials and Technology*, vol. 99, no. 1, p. 2, 1977.

[54] V. Tvergaard, "Influence of Voids on Shear Band Instability Under Plane Strain Conditions," *International Journal of Fracture*, vol. 17, no. 4, pp. 389–407, 1981.

[55] C. C. Chu and A. Needleman, "Void Nucleation Effects in Biaxially Stretched Sheets," *Journal of Engineering Materials and Technology*, vol. 102, no. 3, p. 249, 1980.

[56] M. Fourmeau, T. Børvik, A. Benallal, O. G. Lademo, and O. S. Hopperstad, "On the plastic anisotropy of an aluminium alloy and its influence on constrained multiaxial flow," *International Journal of Plasticity*, vol. 27, no. 12, pp. 2005–2025, 2011.

[57] M. Fourmeau, T. Børvik, A. Benallal, and O. S. Hopperstad, "Anisotropic failure modes of high-strength aluminium alloy under various stress states," *International Journal of Plasticity*, vol. 48, pp. 34–53, 2013.

[58] F. Barlat, H. Aretz, J. W. Yoon, M. E. Karabin, J. C. Brem, and R. E. Dick, "Linear transfomation-based anisotropic yield functions," *International Journal of Plasticity*, vol. 21, no. 5, pp. 1009–1039, 2005.

[59] S. M. Keralavarma and A. A. Benzerga, "A constitutive model for plastically anisotropic solids with non-spherical voids," *Journal of the Mechanics and Physics of Solids*, vol. 58, no. 6, pp. 874–901, 2010.

[60] L. Morin, J. B. Leblond, and D. Kondo, "A Gurson-type criterion for plastically anisotropic solids containing arbitrary ellipsoidal voids," *International Journal of Solids and Structures*, vol. 77, pp. 86–101, 2015.

[61] R. Hill, "A theory of the yielding and plastic flow of anisotropic metals," *Proceedings of the Royal Society of London A: Mathematical, Physical and Engineering Sciences*, vol. 193, no. 1033, pp. 281–297, 1948.

[62] Dassault Systèmes Simulia, "Abaqus 6.14 / Analysis User's Guide," 2014.

[63] S. Basu and A. Benzerga, "On the path-dependence of the fracture locus in ductile materials: Experi-

ments," *International Journal of Solids and Structures*, vol. 71, pp. 79–90, oct 2015.

[64] T. Børvik, O. S. Hopperstad, and K. O. Pedersen, "Quasi-brittle fracture during structural impact of AA7075-T651 aluminium plates," *International Journal of Impact Engineering*, vol. 37, no. 5, pp. 537–551, 2010.

[65] A. V. Hershey, "The plasticity of an isotropic aggregate of anisotropic face-centered cubic crystals," *Journal of Applied Mechanics*, vol. 21, pp. 241–249, 1954.

[66] W. F. Hosford, "A Generalized Isotropic Yield Criterion," *Journal of Applied Mechanics*, vol. 39, pp. 241–249, 1972.

[67] T. Pardoen and J. W. Hutchinson, "Extended model for void growth and coalescence," *Journal of the Mechanics and Physics of Solids*, vol. 48, no. 12, pp. 2467–2512, 2000.

[68] S. M. Keralavarma and S. Chockalingam, "A criterion for void coalescence in anisotropic ductile materials," *International Journal of Plasticity*, vol. 82, pp. 159–176, 2016.

[69] M. E. Torki, C. Tekoglu, J. B. Leblond, and A. A. Benzerga, "Theoretical and numerical analysis of void coalescence in porous ductile solids under arbitrary loadings," *International Journal of Plasticity*, vol. 91, pp. 160–181, 2017.